PAPER • **OPEN ACCESS**

Robust adaptive compensation of force-based RTHS testing with uncertain compliance spring and force measurement noise

To cite this article: Diego Araya and Gastón Fermandois 2024 *J. Phys.: Conf. Ser.* **2647** 142008

Journal of Physics: Conference Series **2647** (2024) 142008 doi:10.1088/1742-6596/2647/14/142008

Robust adaptive compensation of force-based RTHS testing with uncertain compliance spring and force measurement noise

Diego Araya
M.Sc. Student, Universidad Técnica Federico Santa María, Santiago, Chile
E-mail: diego.arayai@alumnos.usm.cl

Gastón Fermandois
Assistant Professor, Universidad Técnica Federico Santa María, Valparaíso, Chile
E-mail: gaston.fermandois@usm.cl

Abstract.
This study proposes a force-based real-time hybrid simulation (RTHS) framework with robust compliance-based adaptive compensation. Adding a compliance spring between the loading actuator and a rigid specimen is an alternative to measure restoring forces through load cells with significant noise. But, we considered compliance spring and load cell properties to be uncertainties. Robust adaptive model-based compensation will be employed to overcome force-tracking errors between substructures. The proposed methodology will be verified in a virtual RTHS environment, where parametric studies will be considered to check the system's robustness over uncertain compliance and specimen properties.

1. Introduction

Real-time hybrid simulation (RTHS) [1] is a powerful tool that combines a numerical computer simulation of a structure subjected to recorded seismic accelerations with an experimental test in the laboratory. This form of structural analysis has proven to be a very effective and low-cost technique compared to other proposed methodologies: only one physical component is required as a test specimen (e.g., columns or MR dampers), instead of building a complete structure in the laboratory.

This technique has made significant progress in recent years [2, 3]. To carry out the simulation, the structure under study is separated into a numerical substructure (NS), which will be evaluated using a numerical simulation on a computer, and an experimental substructure (ES), which is tested in the laboratory using a transfer system (e.g., shake tables or servo-hydraulic actuators). The most used methodology for an RTHS test is based on command displacements from the NS to the actuator and measuring forces from the specimen that return to the NS as inputs to complete the hybrid loop. The boundary conditions of displacement compatibility and force equilibrium must be satisfied to validate the simulation. On the other hand, force-based hybrid testing consists of commanding forces from the NS to the actuator, which applies them

on the specimen, from where the measured states (position, velocity, and acceleration) return as input to the NS.

One of the first experimental force-based tests was the *Effective Force Testing* (EFT) proposed by Dimig et al. [4]. In this study, the forces that are applied by the actuators can be calculated *offline* since the seismic record is known before the test, and the entire structure is experimentally tested. EFT checks the possibility of commanding forces by an actuator. Still, problems with the natural velocity feedback studied by Dyke et al. [5], and limitations with the servo-valve and actuator capacities were evidenced.

Moreover, in a force-based test, low-magnitude displacement errors (compatibility) in the simulation could have the effect of significant errors in measured forces (equilibrium), leading the simulation to numerical and experimental instabilities. Shao [6] proposed the *Real-time Dynamic Hybrid Testing scheme* (RTDHT) with a novel solution developed by Sivaselvan [7], consisting of introducing a *compliance spring* between the piston and the test specimen. This idea is initially proposed by Pratt [8] for a robotic force control. The main goal of the compliance spring is to add flexibility to the system. Then, the controller can be formulated in a displacement-based environment, while forces are still commanded from the NS as input to the controller. In addition, the force can be measured by load cells or using Hooke's Law (i.e., measuring the elongation of the spring with a displacement transducer and multiplying by its elastic stiffness).

The literature provides some examples of hybrid testing with compliance springs. Chae [9] compare simulations with force-based and displacement-based compensation using his designed Adaptive Time Series Compensation (ATS) [10]. In this study, a proposal made by Chae is to use a beam as a compliance element when axial loads are applied on large-scale test structures. The beam must be designed to ensure its linear elastic behavior works as a spring. Later, Chae [11] implement EFT with ATS compensation and a compliance frame attached to non-linear structures and verify the advantages of the EFT for large-scale structures with a force control scheme.

On the other hand, different dynamic compensation methods have been developed for RTHS tests and are available to reduce the synchronization error between commanded and measured signals. Most methods assume a constant time delay of the transfer system [12]. However, the time delay is affected by the interaction between the actuator and the specimen. This issue is known as control-structure interaction [5]. Later, novel compensation schemes were developed. Carrion [13] proposes a method based on the servo-hydraulic and the physical specimen model, known as model-based compensation.

In this paper, we study a force-based RTHS of a high-stiffness specimen and a compliance spring to add flexibility to the test setup. To allow good synchronization between substructures, a robust adaptive model-based compensator will be formulated to work in a force-based environment. This formulation will consider uncertainty in the dynamic properties of the specimen and compliance spring, and the effects of load cell measurement noise. The performance of the robust compensator will be compared with the traditional model-based compensator through a series of virtual tests using a modified version of the RTHS benchmark problem.

2. Problem formulation

2.1. Reference structure

The reference structure (RS) is a three-story one-bay lumped-mass shear building. It is modeled as a linear time-invariant system, with three lateral degrees of freedom (DOF) on each floor level. A shear wall is mounted between the ground and the first story to add stiffness to the first story DOF, and, consequently, to the entire system. The equation of motion (EOM) that represents the dynamics of the RS, defined in a domain $\mathbf{\Omega}$ is:

$$\mathbf{\Omega}: \quad \mathbf{M}\ddot{\mathbf{x}}(t) + \mathbf{C}\dot{\mathbf{x}}(t) + \mathbf{K}\mathbf{x}(t) = \mathbf{p}(t) \tag{1}$$

where $\mathbf{M}$, $\mathbf{C}$, and $\mathbf{K}$ are the mass, damping, and stiffness matrices, respectively. $\mathbf{x}(t) = \{x_1(t), x_2(t), x_3(t)\}^T \in \mathbb{R}^n$ is the displacement vector relative to the ground. $\dot{\mathbf{x}}(t) \in \mathbb{R}^n$ and $\ddot{\mathbf{x}}(t) \in \mathbb{R}^n$ are the velocity and acceleration vectors obtained from the respective time derivatives from $\mathbf{x}(t)$. $\mathbf{p}(t)$ is the external load vector. For this problem, $\mathbf{p}(t) = -\mathbf{M}\boldsymbol{\Gamma}\ddot{x}_g$, where $\boldsymbol{\Gamma} = \{1, 1, 1\}^T$ is the seismic participation vector, and $\ddot{x}_g(t)$ is the ground acceleration.

The initial conditions for this problem are $\mathbf{x}(0) = \dot{\mathbf{x}}(0) = \{0, 0, 0\}^T$. The chosen RS is a simple model of the scaled three-story test structure used in several RTHS previous studies [14, 15]. The mass $\mathbf{M}$ and stiffness $\mathbf{K}$ matrices are the following:

$$\mathbf{M} = \begin{bmatrix} m_1 & 0 & 0 \\ 0 & m_2 & 0 \\ 0 & 0 & m_3 \end{bmatrix}; \ \mathbf{K} = \begin{bmatrix} k_1 + k_2 + k_w & -k_2 & 0 \\ -k_2 & k_2 + k_3 & -k_3 \\ 0 & -k_3 & k_3 \end{bmatrix} \tag{2}$$

where m_i and k_i are the mass and stiffness of each story, and k_w is the wall stiffness. Subscript $i = \{1, 2, 3\}$ denotes the story number. The damping matrix $\mathbf{C}$ is obtained employing modal damping with the following damping ratios $\zeta_i = \{0.31, 0.62, 0.63\}[\%]$ for the three modes [15]. $\mathbf{C}$ matrix is calculated as $\mathbf{C} = (\boldsymbol{\Phi}^T)^{-1}\text{diag}(2\zeta\omega_{n1}m_1^*, 2\zeta\omega_{n2}m_2^*, 2\zeta\omega_{n3}m_3^*)(\boldsymbol{\Phi})^{-1}$, with m_i^* and ω_{ni} the modal mass and natural frequencies respectively. $\boldsymbol{\Phi}$ is the mode shape matrix. A stiffness ratio between the wall and columns of 20 is considered for the wall stiffness design, which is added to the DOF 1 in the stiffness matrix $\mathbf{K}$. The fundamental frequencies of the RS are $f_n = \{8.02, 21.3, 54.5\}[\text{Hz}]$. Mass and stiffness values for each story are shown in Table 1.

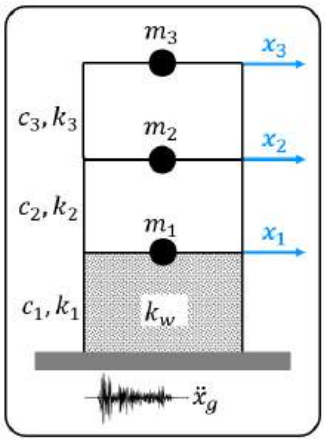

Figure 1: Reference structure.

Table 1: Reference structure parameters.

Story (DOF)	**Mass** [kN · s^2/mm]	**Stiffness** [kN/mm]
1	$98.3 \cdot 10^{-6}$	10.79
2	$98.3 \cdot 10^{-6}$	0.686
3	$98.3 \cdot 10^{-6}$	0.684

2.2. Substructuring method

A method known as substructuring is used to divide the domain $\boldsymbol{\Omega}$ of the reference structure into smaller partitions that are coupled and can be solved independently. However, the coupling between the partitions must be included in the motion equations as boundary conditions. In this case, the RS is divided into two substructures, denominated Numerical (NS) and Experimental (ES) substructures, with domains $\boldsymbol{\Omega}^N$ and $\boldsymbol{\Omega}^E$ respectively. Thus, the RS can be defined now as the union of the subdomains generated $\boldsymbol{\Omega} = \boldsymbol{\Omega}^N \cup \boldsymbol{\Omega}^E$. Furthermore, the response of the reference structure can be obtained by combining the responses obtained from solving the coupled motion equations of each substructure. The coupled numerical and experimental equations of motion are shown in Eq.(3) and (4), respectively. Additionally, Figure 1 shows the substructuring scheme for this study. The wall is considered an element that only adds stiffness to the system. The

wall's mass compared to the mass of each floor is considered negligible and is not included in the equations.

$$\mathbf{\Omega}^N : \mathbf{M}^N\ddot{\mathbf{x}}^N + \mathbf{C}^N\dot{\mathbf{x}}^N + \mathbf{K}^N\mathbf{x}^N = \mathbf{p}^N + \mathbf{g}^N \tag{3}$$

$$\mathbf{\Omega}^E : \mathbf{M}^E\ddot{\mathbf{x}}^E + \mathbf{C}^E\dot{\mathbf{x}}^E + \mathbf{K}^E\mathbf{x}^E = \mathbf{p}^E + \mathbf{g}^E \tag{4}$$

Superscripts N and E are used to identify the numerical and experimental substructures, respectively. The vectors $\mathbf{g}^N = \{\mathbf{g}_i^N, \mathbf{g}_b^N\}^T$ and $\mathbf{g}^E = \{\mathbf{g}_i^E, \mathbf{g}_b^E\}^T$ are the coupling force vectors between both domains, applied to their respective substructure, where the subscripts "i" and "b" indicate interior and boundary DOF, respectively. Assuming that the subdomains are only coupled on the boundary DOF 1, then the internal coupling forces are equaled to zero $\mathbf{g}_i^N = \mathbf{0}_i^N$ and $\mathbf{g}_i^E = \mathbf{0}_i^E$. With the previous assumption, the resulting boundary conditions for this problem are displacement compatibility and force equilibrium, shown in Eq.(5).

$$\mathbf{x}_b^N = \mathbf{x}_b^E \; ; \quad \mathbf{g}_b^N + \mathbf{g}_b^E = \mathbf{0}_b \tag{5}$$

The reference EOM in Eq.(1) is separated into numerical and experimental components as in Eq.(6). The parameters and the DOF are associated with each partition using superscript N and E, and story subscript i.

$$\begin{gathered}\begin{bmatrix} m_1^E & 0 & 0 \\ 0 & m_2^N & 0 \\ 0 & 0 & m_3^N \end{bmatrix}\begin{Bmatrix} \ddot{x}_1^E \\ \ddot{x}_2^N \\ \ddot{x}_3^N \end{Bmatrix} + \begin{bmatrix} c_{11}^E & c_{12}^N & c_{13}^N \\ c_{21}^N & c_{22}^N & c_{23}^N \\ c_{31}^N & c_{22}^N & c_{33}^N \end{bmatrix}\begin{Bmatrix} \dot{x}_1^E \\ \dot{x}_2^N \\ \dot{x}_3^N \end{Bmatrix} + \\ \begin{bmatrix} k_1^E + k_2^N & -k_2^N & 0 \\ -k_2^N & k_2^N + k_3^N & -k_3^N \\ 0 & -k_3^N & k_3^N \end{bmatrix}\begin{Bmatrix} x_1^E \\ x_2^N \\ x_3^N \end{Bmatrix} = -\begin{bmatrix} m_1^E & 0 & 0 \\ 0 & m_2^N & 0 \\ 0 & 0 & m_3^N \end{bmatrix}\begin{Bmatrix} 1 \\ 1 \\ 1 \end{Bmatrix}\ddot{x}_g\end{gathered} \tag{6}$$

From Eq.(6), the numerical substructure is separated from the experimental one since they will be solved separately, resulting in the following two EOM:

$$\begin{gathered}\begin{bmatrix} m_2^N & 0 \\ 0 & m_3^N \end{bmatrix}\begin{Bmatrix} \ddot{x}_2^N \\ \ddot{x}_3^N \end{Bmatrix} + \begin{bmatrix} c_{22}^N & c_{23}^N \\ c_{22}^N & c_{33}^N \end{bmatrix}\begin{Bmatrix} \dot{x}_2^N \\ \dot{x}_3^N \end{Bmatrix} + \begin{bmatrix} k_2^N + k_3^N & -k_3^N \\ -k_3^N & k_3^N \end{bmatrix}\begin{Bmatrix} x_2^N \\ x_3^N \end{Bmatrix} = \\ \underbrace{-\begin{bmatrix} m_2^N & 0 \\ 0 & m_3^N \end{bmatrix}\begin{Bmatrix} 1 \\ 1 \end{Bmatrix}\ddot{x}_g}_{\mathbf{p}^N} \underbrace{-\begin{Bmatrix} c_{21}^N \\ c_{31}^N \end{Bmatrix}\dot{x}_1^E - \begin{Bmatrix} -k_2^N \\ 0 \end{Bmatrix}x_1^E}_{\mathbf{g}_b^N}\end{gathered} \tag{7}$$

$$m_1^E\ddot{x}_1^E + c_1^E\dot{x}_1^E + k_1^E x_1^E = \underbrace{-m_1^E\ddot{x}_g}_{\mathbf{p}^E} + \underbrace{c_2^N(\dot{x}_2^N - \dot{x}_1^E) + k_2^N(x_2^N - x_1^E)}_{\mathbf{g}_b^E} \tag{8}$$

The motion equations shown are consistent with the force-based substructuring performed by [6]. However, only actuators will be used as the transfer system in this case. Additionally, each equation denotes contributions from external forces $\mathbf{p}$ and from coupling forces $\mathbf{g_b}$. Figure 2 shows the closed hybrid loop used in this study. In summary, the coupling force $\mathbf{g}_b^N$ at the boundary DOF is obtained from the numerical substructure, which is imposed on the specimen through a transfer system. The position and velocity of the specimen are measured and fed back as input to the numerical substructure, closing the hybrid loop.

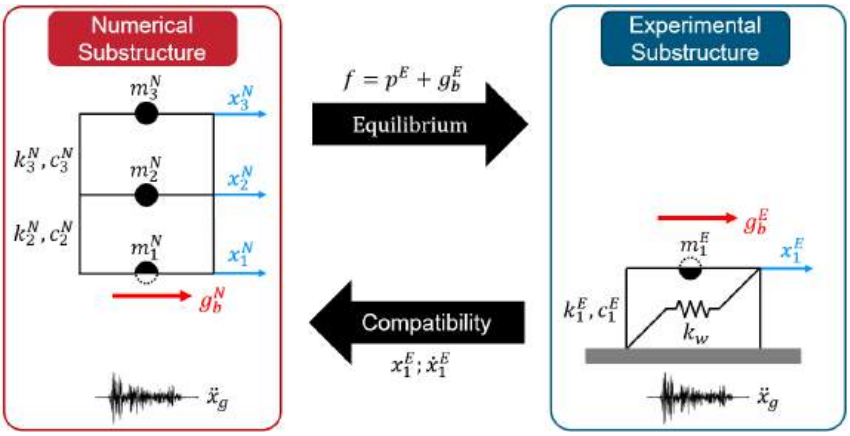

Figure 2: Hybrid loop for a force-based RTHS test.

2.3. Virtual simulation cases

The simulations will be conducted virtually using Matlab R2023a and Simulink software. The numerical substructure is incorporated in its state-space form, while transfer functions represent the experimental components. Figure 3 shows a block diagram of the implementation of FBRTHS in Simulink. The system will be subjected to the seismic record of El Centro on May 19th, 1940, NS component, scaled at 80% of its PGA. A fourth-order Runge-Kutta solver with a fixed time step is used to solve the numerical integration, considering a sampling frequency of $f_s = 4,096[Hz]$, and a sampling time of $\Delta t = 1/f_s$.

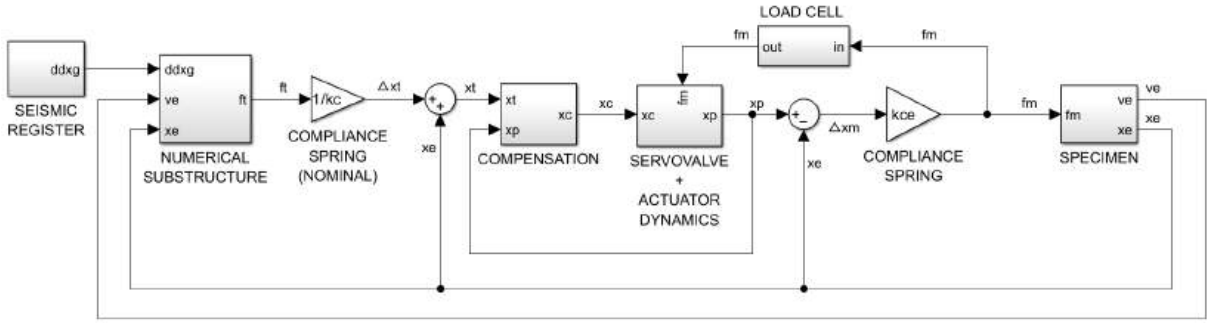

Figure 3: FBRTHS simulink implementation.

2.4. Evaluation criteria

The results will be evaluated according to the following criteria:

- J_2: The normalized root-mean-square error (NRMSE) between the target displacement x^t and the measured displacement x^m is used to measure the synchronization error between the displacements caused by the transfer system.
- A_2: The normalized root-mean-square error (NRMSE) between the target force signal f^t and the measured force signal f^m is used to measure the synchronization error between the mentioned forces. It is equivalent to the J_2 criterion for displacements.
- τ_d: Time delay between target and measured signal, obtained in the frequency domain [16]. Its unit is [ms].

$$J_2 = \sqrt{\frac{\sum_{l=1}^{L}(x^m[l] - x^t[l])^2}{\sum_{l=1}^{L}(x^t[l])^2}}; \quad A_2 = \sqrt{\frac{\sum_{l=1}^{L}(f^m[l] - f^t[l])^2}{\sum_{l=1}^{L}(f^t[l])^2}} \tag{9}$$

Where l is the discrete time index and L is the total number of elements in the vector (force or displacement).

3. Transfer system

To impose the force coming from the numerical substructure onto the specimen, a transfer system is used, which is composed of the actuator, the servo-valve, the piston, and sensors that measure displacement and force. The components of the transfer system are modeled as linear systems, which allows them to be represented as transfer functions in the Laplace domain. The interaction between the actuator and the specimen defines the control plant. The dynamics of the control plant are shown as a block diagram in Figure 4, where the input signal is f^t and the outputs are the measured displacement from the piston x^p, the specimen displacement x^m, and the measured force f^m.

As previously mentioned, the actuator is a nonlinear system with a stiff oil column designed to be operated based on displacement control [17]. However, since the specimen corresponding to the first floor has high rigidity due to the wall, it is expected that the measured displacements will have a very low order of magnitude. Noise could contaminate the measured displacement signal, causing errors that generate large values and variations in the restorative force, causing the boundary conditions not to be satisfied in the integration time, and producing drag errors that can lead the test to numerical instability. In addition, given the rigid nature of the specimen, there are problems in the interaction between the piston and the specimen due to the connection, as well as the friction between the elements that compose it. One option for the aforementioned difficulties is to implement a force control methodology. However, similar problems arise as those already mentioned.

As a solution, it is chosen to incorporate a compliance spring between the piston and the specimen [7], which primarily adds flexibility to the system and allows the actuator to be controlled based on displacements, while the simulation is resolved based on a force scheme, as shown in Figure 4, where the signal f^t coming from the numerical substructure is divided by the stiffness of the spring k_c. Since both ends of the spring will displace, it is possible to calculate a target displacement x^t, from the relative displacement of the DOF of the spring as $\Delta x = x^t - x^e \Rightarrow x^t = \Delta x + x^e$. Thus, the target force f^t is transformed into a displacement x^t, which after passing through the transfer system, will be measured from the end of the piston that connects with the spring, x^p, as shown in the implementation scheme of the control plant in Figure 5. Then, the displacement of the specimen is subtracted from the displacement of the piston to obtain Δx^m, which yields the measured force f^m when multiplied by the spring stiffness. Therefore, through displacement control, it is also possible to impose the target force.

The spring chosen for this study has mechanical properties that allow it to function in the linear elastic range throughout the test. In addition, the spring cannot be too flexible (very low stiffness) compared to the specimen since, to achieve the commanded displacement, the piston must perform a more significant displacement with a higher velocity, which can lead to instability in the simulation. It is also possible for the actuator to break down by commanding a displacement for which it was not designed since it exceeds its limit. On the contrary, adding a spring with a stiffness similar to or higher than the specimen leads to numerical instability since the piston displacement tends to be null. Thus, the spring stiffness of choice allows the actuator not to exceed the benchmark problem's limitations [18] and ensures simulation stability.

Since this work will be realized in a virtual format, a parametric transfer system model must be implemented computationally. A simplified actuator model used in previous studies [15] is chosen and adapted to be implemented in this framework. The control plant parameters are

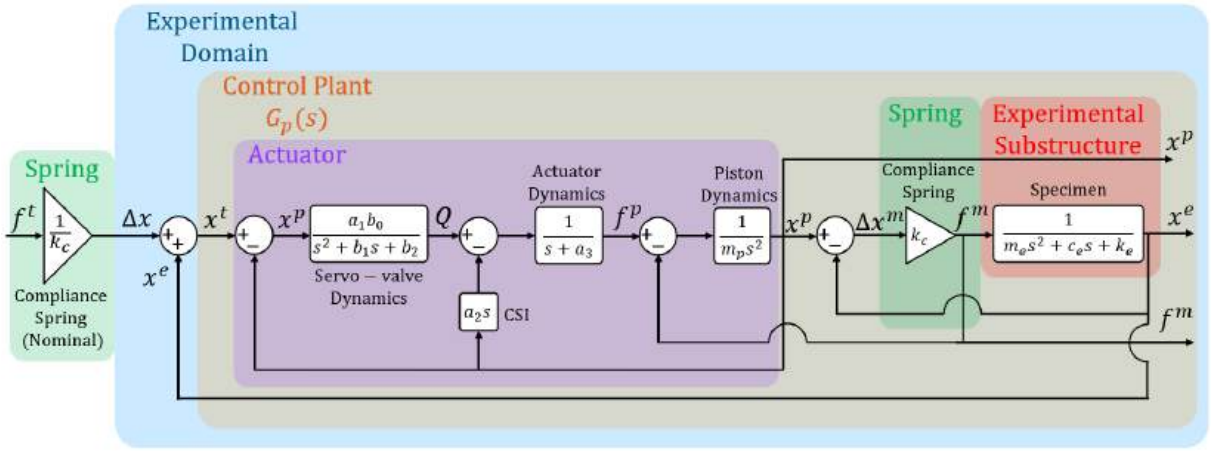

Figure 4: Block diagram of the control plant.

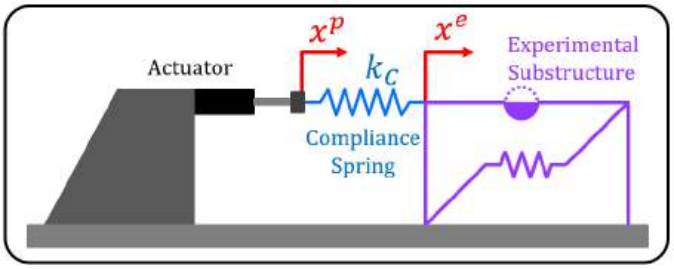

Figure 5: Implementation of the compliance spring.

shown in Table 2, where the values for the actuator are obtained from the benchmark problem developed by Silva et al.[18]. In this case, the uncertainty of the actuator parameters is not considered since it will be incorporated into the stiffness of the compliance spring and the load cell.

By replacing the parameters in Table 2 in their respective control plant blocks shown in Figure 5, we obtain the transfer function of the control plant $G_p(s)$ shown in Eq.(10). This TF has all its five poles on the left-hand side of the imaginary plane.

Table 2: Experimental domain parameter values.

Parameter	Value	Unit	Parameter	Value	Unit
$a_1\beta_0$	$2.13 \cdot 10^7$	MPa· mm/s	m_p	$1 \cdot 10^{-}6$	kN· s^2/mm
a_2	4.23	MPa·mm	m_e	$98.3 \cdot 10^{-}6$	kN· s^2/mm
a_3	3.3	1/s	c_e	$365.3 \cdot 10^{-}6$	kN· s/mm
β_1	425	–	k_e	10.79	kN/mm
β_2	10^5	1/s	k_c	0.5397	kN/mm

Since compensations will be designed based on the model, an estimation of the control plant is performed considering only three poles, with no zeros, to incorporate them in a simplified way into the design of the controllers. The estimation is performed using Matlab R2023a software in the time domain, using a chirp input ranging from 0.1[Hz] to 20[Hz] to capture the system

dynamics in the frequency range typically used in RTHS studies. The obtained transfer function G_p^{est} is shown in Eq.(11), and achieves a 99.97% fit to $G_p(s)$.

$$G_p(s) = \frac{2.13 \cdot 10^{13}}{s^5 + 428.3 \cdot s^4 + 4.764 \cdot 10^6 \cdot s^3 + 1.983 \cdot 10^9 \cdot s^2 + 4.670 \cdot 10^{11} \cdot s + 2.152 \cdot 10^{13}} \quad (10)$$

To demonstrate the behavior of the control plant, we obtain the Bode diagrams and the poles and zeros of the actuator alone $G_p^{ini}(s)$, the actuator with the specimen considered as a spring (gain) $G_p^e(s)$, the actuator with the specimen and compliance spring $G_p(s)$, and the estimated transfer function $G_p^{est}(s)$. The results are shown in Figure 6. Sequentially, it is observed that $G_p^{ini}(s)$ is the most sensitive representation to the frequency range under study. By adding the rigid specimen, $G_p^e(s)$ shifts downwards, becoming less sensitive to the frequency range and increasing the time delay between the input and output signals. By adding the compliance spring, it is observed that the graph of the system $G_p(s)$ rises again, improving its sensitivity and reducing the time delay.

Finally, it is observed that the graph of $G_p^{est}(s)$ is very similar to $G_p(s)$. This demonstrates that both TFs have similar dynamics in the frequency range under study and validate their use. The same analysis described earlier is observed in the pole-zero plot shown in Figure 6, where it can be seen that the poles of $G_p(s)$ and $G_p^{est}(s)$ are very similar, thus validating the estimation.

$$G_p^{est}(s) = \frac{4.616 \cdot 10^6}{s^3 + 423 \cdot s^2 + 1.009 \cdot 10^5 \cdot s + 4.664 \cdot 10^6} \quad (11)$$

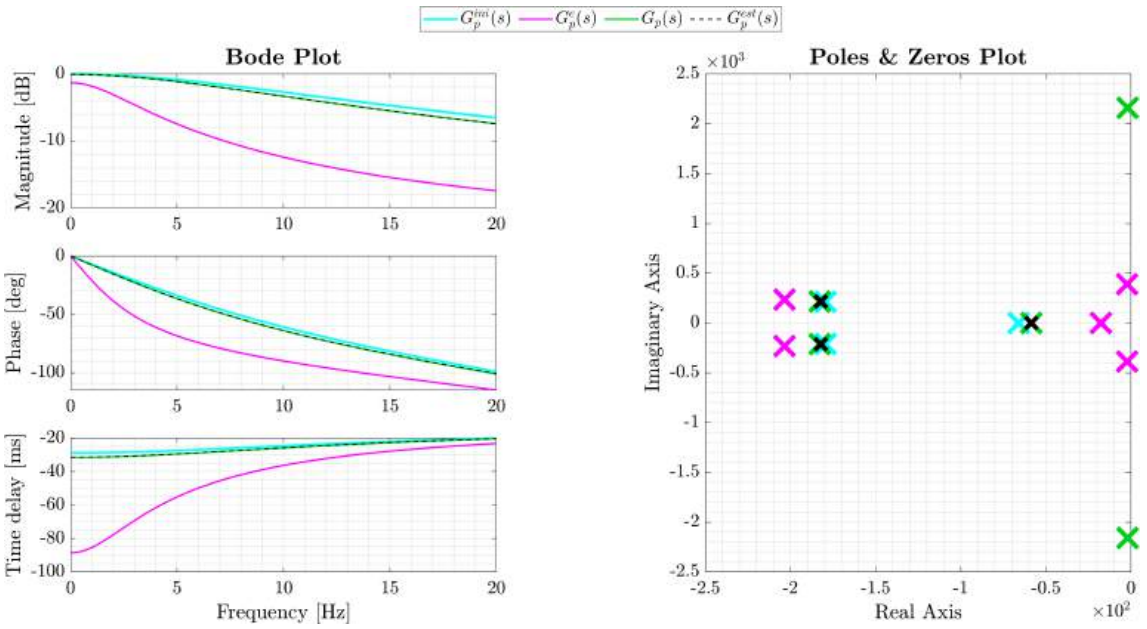

Figure 6: Bode plot, poles, and zeros of described control plants.

4. Compensation

The objective of compensation is to reduce the synchronization errors between the target and measured signals, $x^t - x^m \to 0$. In this study, two types of compensation will be used: inverse feedforward and adaptive model-based (AMBC), to analyze and compare the results obtained with both techniques.

4.1. Inverse feedforward compensation

The objective of using an inverse feedforward compensation is to cancel the actuator dynamics to reduce the tracking error between the signals x^t and x^m, mainly caused by time delays. The design is based on the model-based method proposed by Chen et al. [19] and further developed by Fermandois [20].

Illustratively for the design, the control plant is represented by a third-order transfer function with no zeros, as shown in Eq.(12), where the input and output are denoted as x^t and x^c, respectively. For simplicity, from this point forward, $G_p^{est}(s)$ will be referred to as $G_p(s)$.

$$G_p(s) = \frac{x^m}{x^c} = \left(\frac{1}{a_3 \cdot s^3 + a_2 \cdot s^2 + a_1 \cdot s + a_0} \right) \tag{12}$$

Where a_i, with $i = 1, 2, 3$, are the coefficients of the denominator of the control plant. Therefore, to generate the signal commanded by the compensator x^c from the target signal x^t, the inverse of the control plant $G_p(s)$ must be obtained, as shown in Eq.(13).

$$K_{FF}(s) = G_p^{-1}(s) = \frac{x^c}{x^t} = \left(\frac{a_3 \cdot s^3 + a_2 \cdot s^2 + a_1 \cdot s + a_0}{1} \right) \tag{13}$$

The transfer function $K_{FF}(s)$ obtained is improper because it has 3 zeros and no poles, making its implementation impossible. As a solution, the numerator of $K_{FF}(s)$, which contains terms of time derivatives, is rewritten using the backward difference method, based on Taylor series approximations. In this way, a discrete-time finite impulse response (FIR) filter is obtained, which generates the signal x^c as a higher-order function of time derivatives of the signal x^t. The discrete FIR filter written in the frequency domain is given by:

$$K_{FF}(z^{-1}) = k_0 + k_1 \cdot z^{-1} + k_2 \cdot z^{-2} + k_3 \cdot z^{-3} \tag{14}$$

where z^{-1} is the delay operator and k_i is the discrete feedforward gains. A backward finite differences approximation is employed to estimate time derivatives, which allows calculating the coefficients k_i of Eq.(14) as follows:

$$x_t^{(i)} = \frac{\sum_{i=0}^{n} a_i x_t[k-i]}{b_0}, \quad \forall i = \{0, 1, 2, 3\} \tag{15}$$

Using a sampling frequency of 4,096 [Hz] for the finite approximations, the values of the coefficients k_i obtained for the inverse feedforward compensator are as follows:

$$\mathbf{K}_{ff} = 10^4 \cdot \begin{bmatrix} 1.5692 & -4.5388 & 4.3794 & -1.4097 \end{bmatrix} \tag{16}$$

4.2. Adaptive model-based compensation

The AMBC is designed based on the study conducted by Chen et al. [21], considering the modifications made by Galmez and Fermandois [22]. This compensation technique corresponds to a type of feedforward control, with the difference that the commanded signal is calculated with parameters that change at each time step of the simulation. In contrast, the feedforward compensation designed in the previous section has fixed parameters. The block diagram architecture of the adaptive compensation is shown in Figure 7, where it can be observed that the adaptive block uses the commanded signal x^c and measured signal x^m to calculate the parameters A that will be used in the feedforward block. The controlled signal can be obtained as follows:

$$x^c = AX^t = [a_0 \; a_1 \; a_2 \; a_3] \cdot [x^t \; \dot{x}^t \; \ddot{x}^t \; \dddot{x}^t]^T \tag{17}$$

From Figure 7, A is the vector containing the control parameters, and X^t corresponds to the coefficients of the backward finite difference approximation. This methodology requires initial parameters a_i previously obtained from identifying the transfer system without interaction with the specimen. Thus, the parameters a_i are updated in real-time using the gradient proposed in the study by Chen et al. [21]. The transfer function of the actuator without the specimen and the initial coefficients used in the compensation are shown in Eq. (18).

$$G_p^{ini}(s) = \frac{5.035 \cdot 10^6}{s^3 + 425 \cdot s^2 + 1 \cdot 10^5 \cdot s + 5.035 \cdot 10^6}$$
$$\Rightarrow A^{ini} = (G_p^{ini}(s))^{-1} = \begin{bmatrix} 1 & 1.986 \cdot 10^{-2} & 8.440 \cdot 10^{-5} & 1.986 \cdot 10^{-7} \end{bmatrix} \tag{18}$$

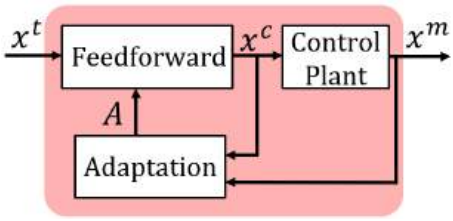

Figure 7: Implementation of the AMBC.

4.3. Adaptive gains optimization

To obtain the adaptive gains, the optimization performed in the displacement-based domain by Galmez and Fermandois [22] is adjusted to be applied in the force-based domain. Figure 8 shows the scheme implemented in Simulink, where the commanded target force signal comes out from the reference structure to the controller, which also receives as input the displacement of the DOF located at the junction between the piston and the compliance spring, x^p.

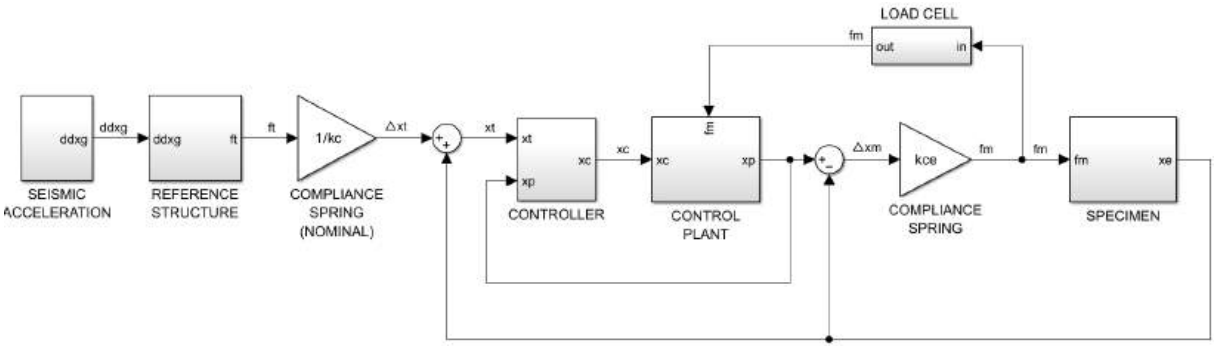

Figure 8: Simulink implementation of the AMBC in open-loop for adaptive gains optimization.

The method employed for obtaining adaptive gains is *Particle Swarm Optimization* [23], with 50 generations considered for a population of 20 particles. One hundred simulations are conducted for each particle, taking into account the uncertainties of each parameter as indicated in Table 3, which are incorporated using the *Latin Hypercube Sampling* Matlab function. The load cell noise in the measurements is represented as a band-limited white noise, where its parameters are defined to obtain a signal-to-noise ratio (SNR) greater than 30[dB]. This value represents that the measured signal is not excessively contaminated by measurement noise.

The objective function corresponds to the indicator R_2, defined as the average synchronization error between the target and measured signals, calculated from the 100 simulations of each particle. The R_2 indicator is calculated as indicated in Eq.(19), where J_2 is the synchronization error defined in Eq.(9).

Table 3: Uncertainty considered for AMBC gains optimization.

Parameter	**Uncertainty**	**Parameter**	**Uncertainty**
M_r, K_r, k_{ce}	$\pm 5[\%]$	m_e	$\{90, 110\} \cdot 10^{-6}[\text{kN} \cdot \text{s}^2/\text{mm}]$
Seismic scales	$\{70, 90\}[\%]$	c_e	$\{340, 380\} \cdot 10^{-6}[\text{kN} \cdot \text{s}/\text{mm}]$
ζ_r	$\{2, 5\}[\%]$	k_e	$\{9, 13\}[\text{kN}/\text{mm}]$

$$R_2(\Gamma_k) = \frac{1}{N} \sum_{i=1}^{N} J_{2,i}(\Gamma_k) \tag{19}$$

The optimization process results in the adaptive gains shown in Eq. (20), with an indicator $R_2 = 4.55\%$. To analyze the optimal solution Γ^*, a neighboring analysis of the adaptive gains is performed, as shown in Fig. 9. The analysis involves fixing two adaptive gains and scanning values with the other two. It is observed that as the values of the adaptive gains increase, the R_2 parameter tends to exceed 100% (yellow zone in plots). The gains are in the stable region, within the range of the R_2 indicator obtained from the optimization.

$$\mathbf{\Gamma}^* = \text{diag}\left(\begin{bmatrix} 10^{4.311} & 10^{5.852} & 10^{2.373} & 10^{-1.726} \end{bmatrix}\right) \tag{20}$$

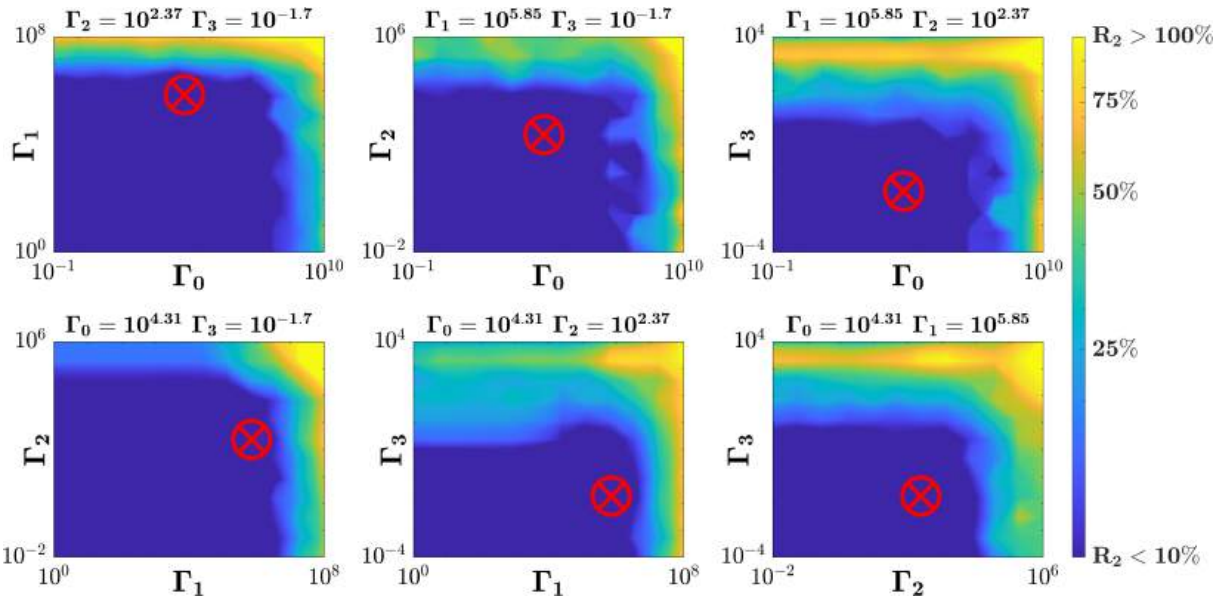

Figure 9: Neighborhood analysis and location of optimal gains obtained from the optimization.

5. Results

5.1. Performance indicators

A hundred simulations were performed for each of the following cases: (i) without compensation; (ii) with inverse feedforward (IFF); and (iii) with adaptive model-based compensations (AMBC). In addition, three levels of uncertainty are considered, both in the numerical structure parameters and in the physical ones: 10%, 20%, and 30%. The results are evaluated using the criteria defined in section 2.4 and the results obtained for the high level of uncertainty considered are shown in Table 4. The obtained indicators show good tracking between the measured signal and the target/reference signal. The inverse feedforward achieves the best result for the indicator $A_2 = 6.99\%$. On the other hand, the best result for the indicator $J_2 = 0.75\%$ and the reduction in time delay $\tau_d = 0.042; [ms]$ are obtained with the AMBC, which did not require prior identification of the control plant, and also achieved the lowest value of J_2, considering that both compensations were designed for displacement control. In general, it is possible to observe in Table 2.4 that both types of compensation can reduce the errors and time delay between the signals.

Table 4: Results obtained considering 30% of uncertainties.

Cases	$\mathbf{A_2}$ [%]	$\mathbf{J_2}$ [%]	$\tau_d[ms]$	**SNR**
Uncontrolled	70.30	61.02	20.07	39.13
IFF	6.99	1.68	0.316	45.01
AMBC	7.49	0.75	0.042	45.77

5.2. Evaluation of controllers

In Figure 10, a boxplot showing the dispersion of the R_2 parameter obtained from 100 simulations is presented, considering the three aforementioned uncertainty levels. The dispersions show that despite the presence of uncertainty in the parameters, both compensations manage to obtain low values of R_2, with the adaptive compensation obtaining the lowest and least dispersed results. It is also observed that as the uncertainty in the parameters increases, the dispersion of the results also increases. However, in the AMBC diagram, the median and the box remain at approximately the same level, while the median of the inverse feedforward increases with greater dispersion.

5.3. Tracking performance

In Figure 11a and 11b, the Synchronization Subspace Plot (SSP) [24] of forces and displacements of the three cases under study are shown, considering a 30% of uncertainty, the graphs show that a better result is obtained in displacement tracking than in force tracking. In both the inverse feedforward and AMBC cases, the force graph is not on the black line, and it is observed that there is only a slight change in slope, indicating that there is still tracking error between the force signals. This result is complementary to the values of the indicator A_2 shown in Table 4, as evidenced by the tracking of the commanded and measured signals.

6. Conclusions

The model-based adaptive controller is tuned and implemented in a virtual real-time hybrid simulation test scheme based on forces using a high-stiffness specimen. It is possible to add flexibility to the system by using a compliance spring between the piston and the specimen. Thus, overcoming the implementation and tracking difficulties that arise in the interaction between

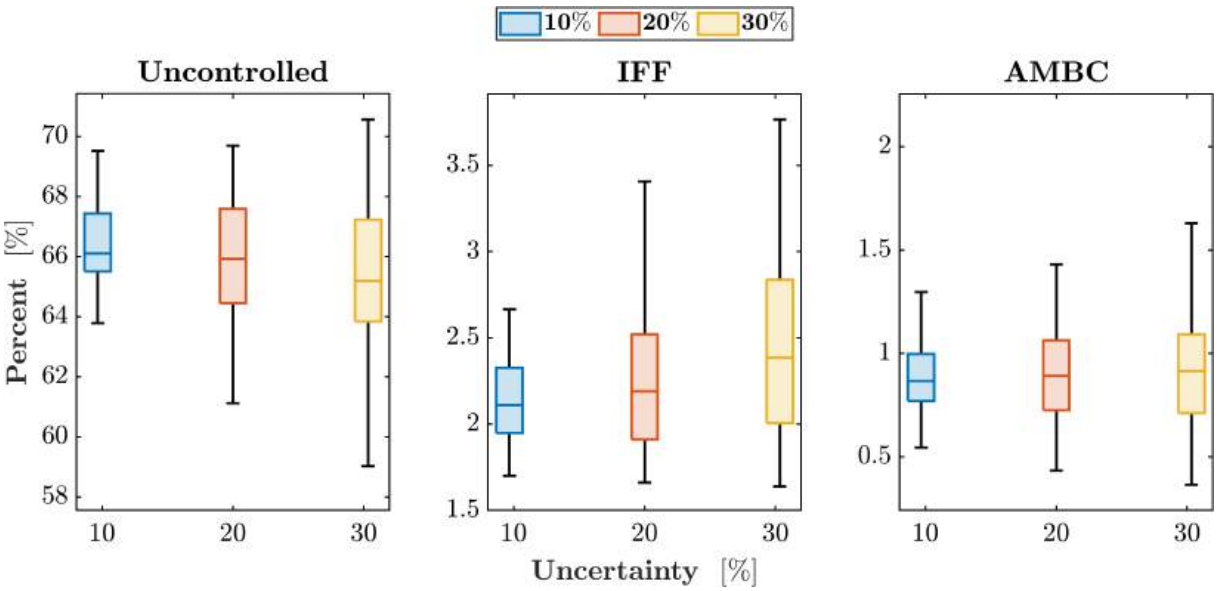

Figure 10: R_2 indicator boxplot for each case.

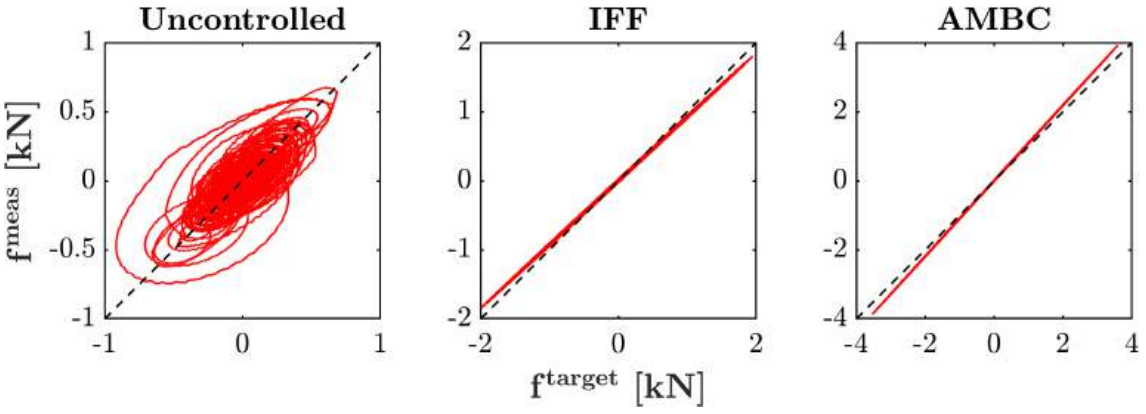

(a) Forces SSP

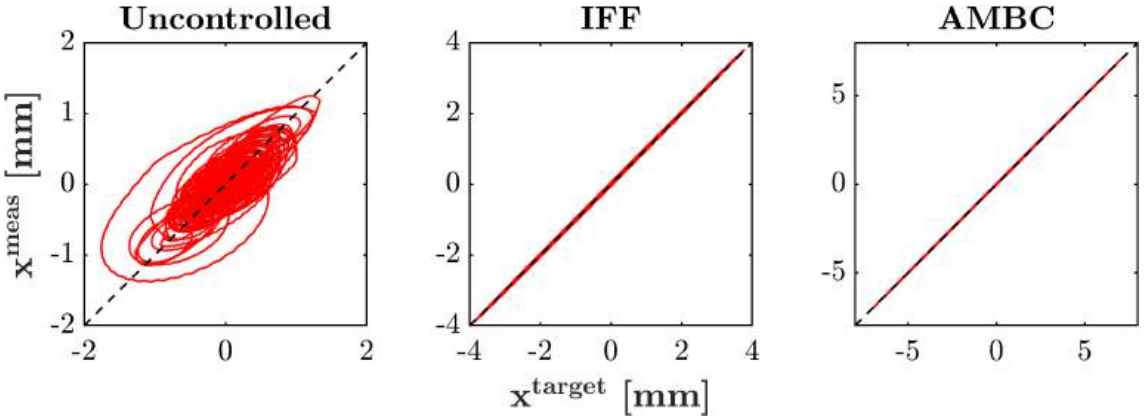

(b) Displacements SSP

Figure 11: Synchronization subspace plots (SSP).

the piston and the rigid substructure is possible. The results show the ability to achieve low tracking error, considering the established levels of uncertainty and noise for each simulation set. Furthermore, the optimization process and design of adaptive gains are adjusted to be implemented in force-based simulations. However, due to the use of the compliance spring, it is possible to perform the optimization process in a displacement-based environment, avoiding measurement and instability issues that occur when testing rigid specimens.

The optimization is performed using the Particle Swarm Optimization method. The results demonstrate the robustness of the AMBC since no prior knowledge of the specimen is required, considering uncertainty in the physical parameters, which eliminates the need for system identification to obtain an estimated transfer function of the control plant.

In future research, it would be interesting to implement this methodology in RTHS tests using multiple actuators, considering different cases, such as a lateral and vertical force or a lateral force and a moment. Additionally, it is possible to study the implementation of the proposed methodology in mixed-mode RTHS tests, combining displacement and force control. It is also suggested to include a compliance spring with nonlinear behavior or another element that could add flexibility to the system, such as a beam.

References

[1] Nakashima M, Kato H and Takaoka E 1992 *Earthquake engineering & structural dynamics* **21** 79–92
[2] Bousias S N 2014 *Journal of Structures* **2014**
[3] Najafi A, Fermandois G A, Dyke S J and Spencer Jr B F 2023 *Engineering Structures* **276** 115–284
[4] Dimig J, Shield C, French C, Bailey F and Clark A 1999 *Journal of Structural Engineering* **125** 1028–1037
[5] Dyke S, Spencer Jr B F, Quast P and Sain M 1995 *Journal of engineering mechanics* **121** 322–338
[6] Shao X and Reinhorn A 2012 *Journal of Earthquake Engineering* **16** 274–295
[7] Sivaselvan M V, Reinhorn A M, Shao X and Weinreber S 2008 *Earthquake Engineering and Structural Dynamics* **37** 1785–1800
[8] Pratt J, Krupp B and Morse C 2002 *Industrial Robot: An International Journal* **29** 234–241
[9] Chae Y, Rabiee R, Dursun A and Kim C Y 2018 *Earthquake engineering & structural dynamics* **47** 854–871
[10] Chae Y, Kazemibidokhti K and Ricles J M 2013 *Earthquake Engineering & Structural Dynamics* **42** 1697–1715
[11] Chae Y and Rabiee R 2018 *Journal of Structural Engineering* **144**
[12] Horiuchi T, Inoue M, Konno T and Namita Y 1999 *Earthquake Engineering & Structural Dynamics* **28** 1121–1141
[13] Carrion J E and Spencer Jr B 2007 Model-based strategies for real-time hybrid testing Tech. rep. Newmark Structural Engineering Laboratory. University of Illinois at Urbana-Champaign
[14] Dyke S J, Spencer Jr B, Sain M and Carlson J 1996 *Smart materials and structures* **5** 565
[15] Phillips B M and Spencer Jr B F 2012 Model-based framework for real-time dynamic structural performance evaluation Tech. rep. Newmark Structural Engineering Laboratory. University of Illinois at Urbana-Champaign
[16] Guo T, Chen C, Xu W and Sanchez F 2014 *Smart materials and structures* **23** 045042
[17] Zhao J, French C, Shield C and Posbergh T 2003 *Earthquake Engineering & Structural Dynamics* **32** 1773–1794
[18] Silva C E, Gomez D, Maghareh A, Dyke S J and Spencer Jr B F 2020 *Mechanical Systems and Signal Processing* **135** 106–381
[19] Chen C and Ricles J M 2009 *Engineering Structures* **31** 2643–2655
[20] Fermandois G and Spencer Jr B F 2018 Development and implementation of a multi-axial real-time hybrid simulation framework Tech. rep. Newmark Structural Engineering Laboratory. University of Illinois at Urbana-Champaign
[21] Chen P C, Chang C M, Spencer B F and Tsai K C 2015 *Bulletin of Earthquake Engineering* **13** 1633–1653
[22] Gálmez C and Fermandois G 2022 *Structural Control and Health Monitoring* **29** e2962
[23] Kennedy J and Eberhart R 1995 *Proceedings of ICNN'95-international conference on neural networks* vol 4 (IEEE) pp 1942–1948
[24] Wallace M, Sieber J, Neild S A, Wagg D J and Krauskopf B 2005 *Earthquake engineering & structural dynamics* **34** 1817–1832